Giovanni De Mari · Marco Domaneschi · Mohammed Ismail · Luca Martinelli · Josè Rodellar

Reduced-order coupled bidirectional modeling of the Roll-N-Cage isolator with application to the updated bridge benchmark

Received: 17 September 2014 / Revised: 26 May 2015 / Published online: 25 June 2015

1 Introduction

A new seismic isolation system, namely the Roll-N-Cage one (RNC in the following), has been recently [14] proposed in the literature. This system incorporates several interesting features and mechanisms in a single unit, among others: isolation, energy dissipation, buffering. It also can provide stiffness against low loading levels (e.g., wind and traffic), a great range of horizontal flexibility, high vertical stiffness and strength for supporting heavy dead loads. Recentering and no uplift during its lateral motion are also interesting features which can be implemented alternatively. As a completion of a previous studies [5,15] on the simulation of the Roll-N-Cage device by uncoupled orthogonal unidirectional models, this work first introduces a reduced-order

G. De Mari · M. Domaneschi (✉) · L. Martinelli
Department of Civil and Environmental Engineering, Politecnico di Milano, P.zza Leonardo da Vinci 32, 20133 Milan, Italy
E-mail: marco.domaneschi@polimi.it
Tel.: +39.02.2399.4267

M. Ismail
Structural Engineering Department, Zagazig University, Zagazig, Egypt

J. Rodellar
Department of Applied Mathematics III, Universitat Politècnica de Catalunya, Barcelona, Spain

coupled bidirectional numerical model of the device. Then the efficiency of such a type of control devices, as simulated by the proposed approach, is evaluated for the seismic protection of cable-supported bridges.

The necessity of a bidirectional formulation stems both from analytical studies, which have highlighted that biaxial structural interaction can significantly affect the seismic response in the nonlinear range, and also from laboratory data which have shown that restoring forces and energy absorbing characteristics of structural elements can be considerably different from those evaluated in uniaxial loading conditions.

This is confirmed also by the results presented herein that show how a coupled bidirectional model is fundamental to precisely estimate the structural response for bidirectional seismic input. In fact, depending on the nature of the bidirectional seismic input, internal forces and structural displacement can change considerably. Furthermore, a reduced bidirectional model of the RNC device has the merit to allow to reproduce accurately the global effect of this type or devices within complex models of structural systems, e.g., bridges or buildings, avoiding the higher computational costs resulting from more detailed representations of the devices.

The case study selected herein is the updated ASCE benchmark model on cable-stayed bridges [2]. The refined bridge model is developed in the ANSYS [1] multipurpose finite element environment so as to include relevant modeling aspects, in the simulation of the stay cables dynamics, in the implementation of the seismic external excitation, in the soil–structure interaction and to compare control strategies for the mitigation of the seismic effects.

The RNC devices are introduced into the finite element numerical model by an external user-element, implemented in an independent executable program called by the main script that controls the analysis in ANSYS. The numerical problem is then solved with a mixed implicit–explicit approach in the time domain through the finite element code solver (Newmark) and, externally to this code, the solution of the differential bidirectional model (Runge–Kutta).

Analyses are carried out in the time domain for a multiple support seismic excitation. The vertical component of the earthquake is considered as well. The seismic input, which consequently is not the same on all the supports, satisfies a fixed coherence function. The soil type regulates the degree of correlation.

2 The RNC device

The Roll-N-Cage (RNC) isolator has been recently proposed [10,14] as an attempt to enhance aseismic design. It is a rolling-based isolation system that allows to achieve the maximum possible structure–ground decoupling and, therefore, to minimize the seismic force transfer to the isolated structure. It provides in a single unit all the necessary functions of vertical rigid support, horizontal flexibility with enhanced stability, hysteretic energy dissipation and resistance to minor vibration loads. Three unique features distinguish the RNC isolator: (1) a self-stopping (buffer) mechanism to limit the isolator displacement under severe seismic excitations to a predetermined value; (2) a linear gravity-based self-recentering mechanism that prevents residual dislocations after earthquakes; and (3) a remarkable ability to resist vertical tension by means of its metallic yield dampers. To obtain the most benefit of the adopted rolling-based motion mechanism, which requires less lateral forces to initiate and maintain a high degree of structure–ground decoupling compared to other motion mechanisms of the elastomeric-based and friction-based isolation systems, the RNC isolator is provided with a lateral pre-yield stiffness mechanism, against minor vibration loads, independent to its bearing mechanism. This independency allows for accurate tuning of the initial pre-yield stiffness to permit the commencement of the seismic isolation process, or structure–ground decoupling, just after the seismic forces exceed the maximum limit of minor vibration loads, contrary to the available isolation systems.

The RNC isolator can be available in different forms to suit the structure or object to be protected regarding mass, size, uni- or multidirectional isolation and the maximum allowed seismic gaps between adjacent structures, as shown in Fig. 1a–c. The RNC isolator was numerically characterized in [15], mathematically modeled in [12], and experimentally investigated in [11] using [13]. Figure 1d, e shows a 1/10 reduced-scale experimental prototype of the design form adequate for light-to-moderate mass structures, at neutral and maximum deformed positions, respectively. Figure 1f depicts the 3D sectional view of the heavy-mass system.

2.1 Self-stopping (buffer) and no-uplift mechanisms of RNC isolator

The self-stopping or buffer mechanism of the RNC isolator is attributable to the two right-angle grooves, which are cut out from the quasi-ellipsoidal core, together with the vertical edge-walls of the upper and lower

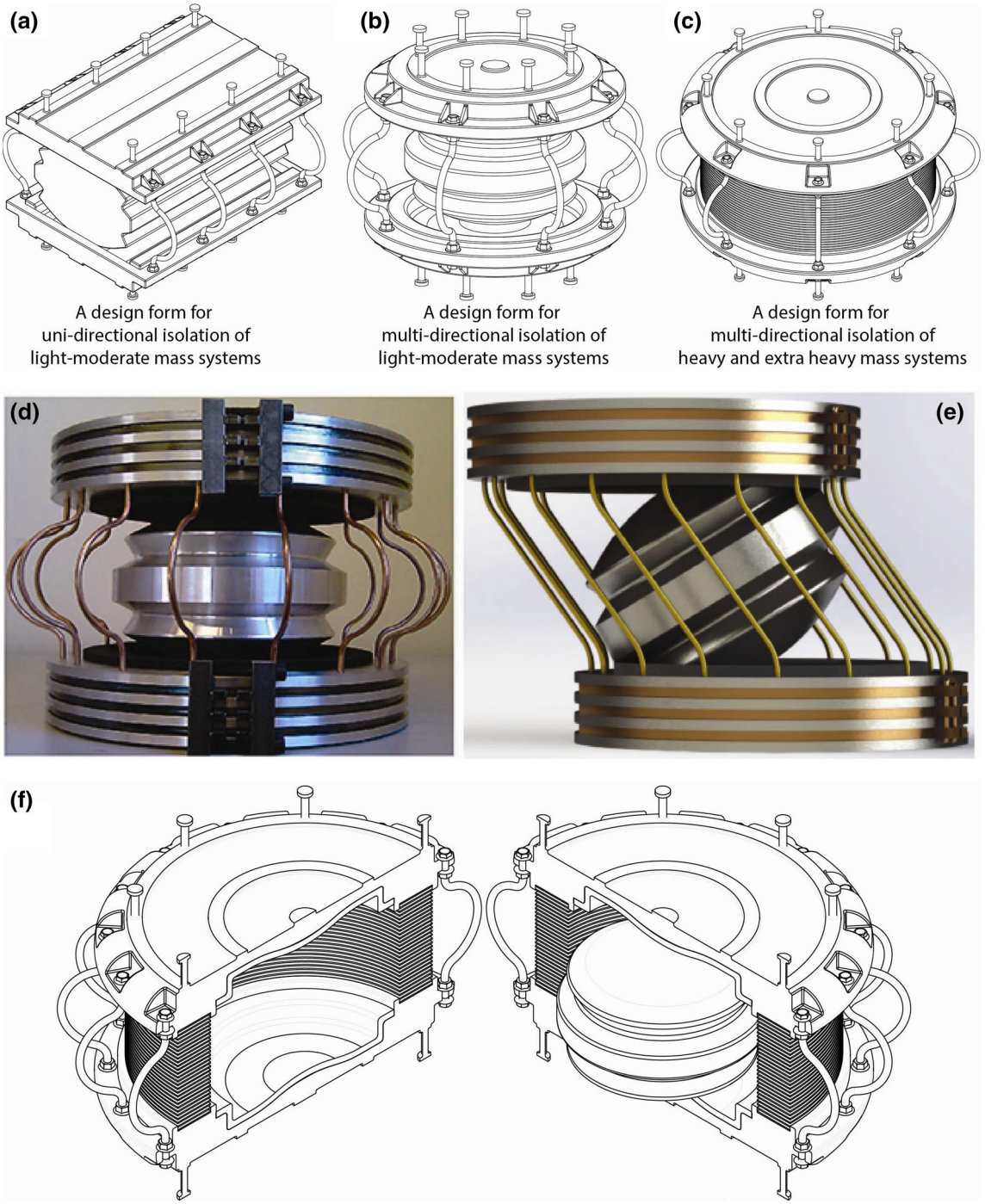

Fig. 1 The RNC isolator: **a** a design form for unidirectional isolation of light–moderate mass systems; **b** a design form for multidirectional isolation of light-moderate mass systems; **c** a design form for multidirectional isolation of heavy and extra heavy mass systems; **d** a small-scale physical prototype at neutral position; **e** a small-scale prototype at maximum deformed position; **f** 3D sectional view of the heavy-mass system

bearing plates, see Fig. 2. Upon reaching the maximum deformed position, a perfect lock is formed smoothly by means of those three components; the core, the upper and lower bearing plates. At that extreme deformed condition, the RNC isolator core works as a restrained, at both ends, inclined rigid link member that allows for no more isolator motion, as shown in Fig. 2a, c. Two main objectives are beyond the integration of the

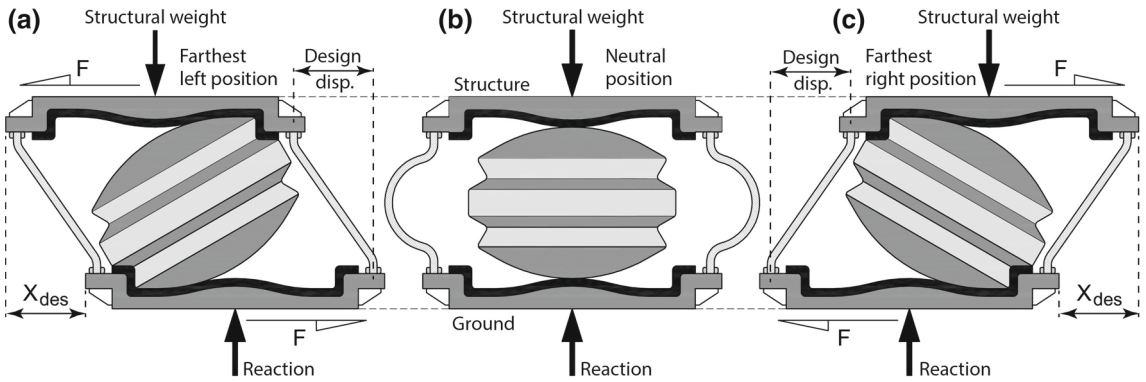

Fig. 2 The self-stopping and no-uplift mechanisms of the RNC isolator

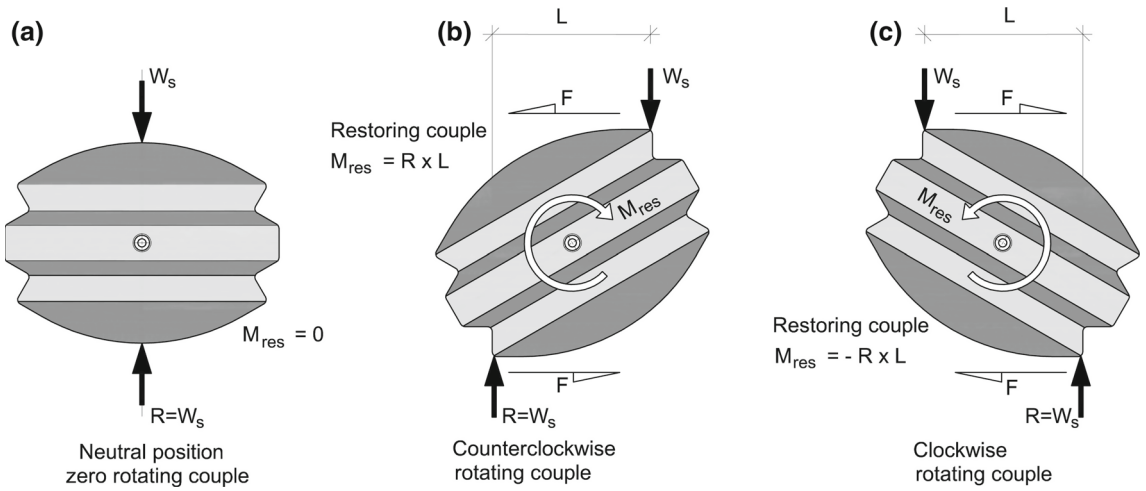

Fig. 3 The self-recentering mechanism of the RNC isolator

buffer mechanism into the RNC isolator. The first objective is to limit the isolator displacement under extreme (low-probability) earthquakes to a previously selected design displacement. The second main objective of the buffer mechanism is to prevent direct seismic pounding of the isolated structure itself with the surrounding adjacent structures in the cases of having insufficient or limited seismic gaps between adjacent structures.

The no-uplift mechanism intends to prevent the generation of vertical displacement and acceleration components out from purely horizontal ones due to rolling of the quasi-ellipsoidal rolling core. Such a no-uplift mechanism is attributed to the inner curvatures of the upper and lower metallic bearing plates (facing the rolling quasi-ellipsoidal core).

2.2 Self-recentering mechanism of RNC isolator

The quasi-ellipsoidal shape of the RNC isolator's rolling core provides an increasing (with lateral deformation) horizontal eccentricity. Such eccentricity generates a restoring couple (together with the superstructure's downward weight and its upward reaction) opposite to the rotating couple to recenter or restore the RNC-isolated structure to its neutral position after excitation with no permanent dislocation, as demonstrated by Fig. 3.

2.3 Hysteretic damping and tension resistance mechanism of RNC isolator

The metallic yield dampers arranged along the outer perimeter of the RNC isolator provide the main source of hysteretic damping and the unique source of notable tension resistance as shown in Fig. 4.

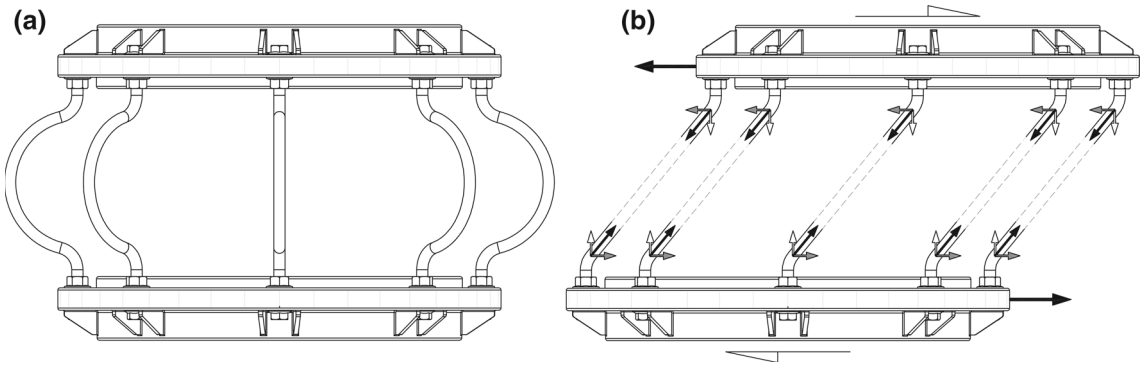

Fig. 4 The hysteretic damping and tension mechanisms of the RNC isolator

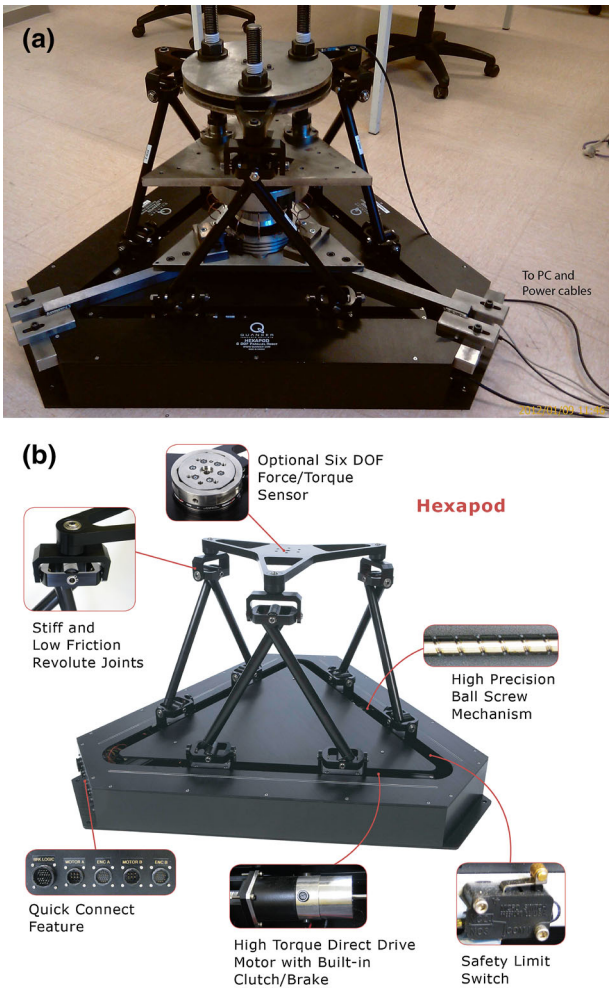

Fig. 5 **a** *Full view* of the Hexapod-based testing machine connected to the controlling PC during testing the RNC isolator. **b** *Dissected view* of the Hexapod (the actuators are hidden into the *lower box* of the machine)

3 Laboratory tests on the physical prototype: a novel testing platform

A novel multipurpose mechanical extension is designed for a Stewart Platform Hexapod as shown in Fig. 5a, b, and later patented [13], to enable the Hexapod (shown in Fig. 6a) to perform up to fifteen standard mechanical tests, besides maintaining its main function as a motion simulator. Figure 6b–d demonstrates one part of the

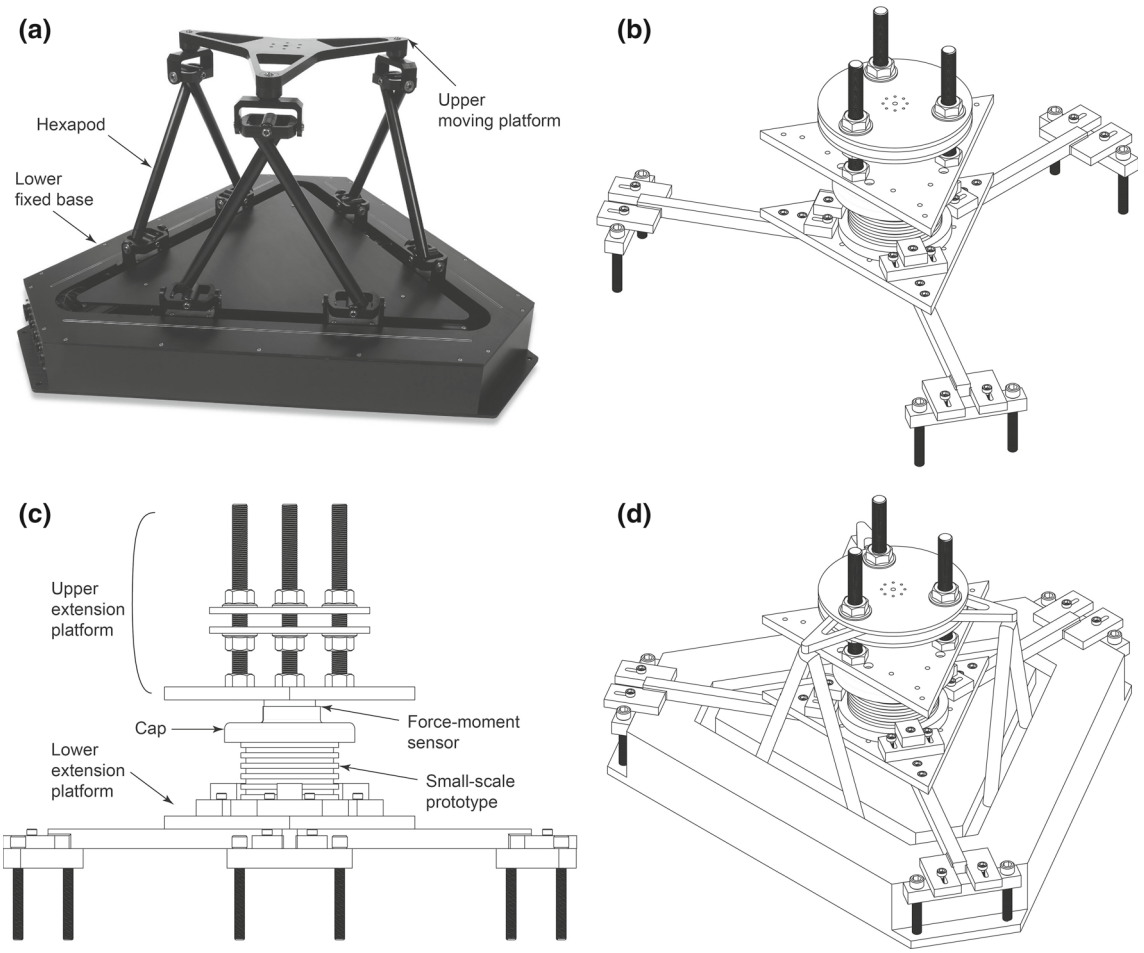

Fig. 6 Mechanical Hexapod extension: **a** Hexapod; **b** *3D view* of the designed Hexapod extension; **c** *elevation view* of the designed Hexapod extension; **d** the designed extension incorporated to Hexapod

designed mechanical extension. This part is suitable for testing experimental block-like, cylindrical and seismic isolation bearing specimens under tension, compression, shear, torsion and fatigue tests. Figure 7a shows a real constructed example of the designed mechanical extension after being integrated to the Hexapod. Some sample real photographs of a RNC isolator experimental prototype under cyclic horizontal shear displacement are shown in Fig. 7 at neutral and different deformed positions. More details about the designed mechanical extension for the Hexapod are found in [13].

A six degrees-of-freedom (DOF) force/torque sensor is used as a load-measuring unit. Alternatively, any other available measuring devices may be used with the developed multipurpose testing platform. The accuracy of the used 6DOF sensor is 0.01 N with a maximum capacity up to 5000 N. After integrating the designed mechanical extension to the Hexapod together with the 6DOF sensor, the resulting Hexapod-based testing machine has the following working ranges and characteristics:

- Maximum acceleration: 1 g;
- Frequency range: 0–20 Hz;
- Dimensions: 1.1, 1.1 (horizontal) and 0.75 (vertical) m;
- Maximum speed (x, y—horizontal—and z—vertical): 0.67, 0.67 and 0.35 m/s;
- Weight: 140 kg;
- Actuator maximum force: 334 N (six actuators);
- Actuator travel: ± 30 m;
- Maximum load: 5000 N;
- Rated power: 1500 W;
- Workspace (displacements in x, y and z): 0.30, 0.30 and 0.19 m;

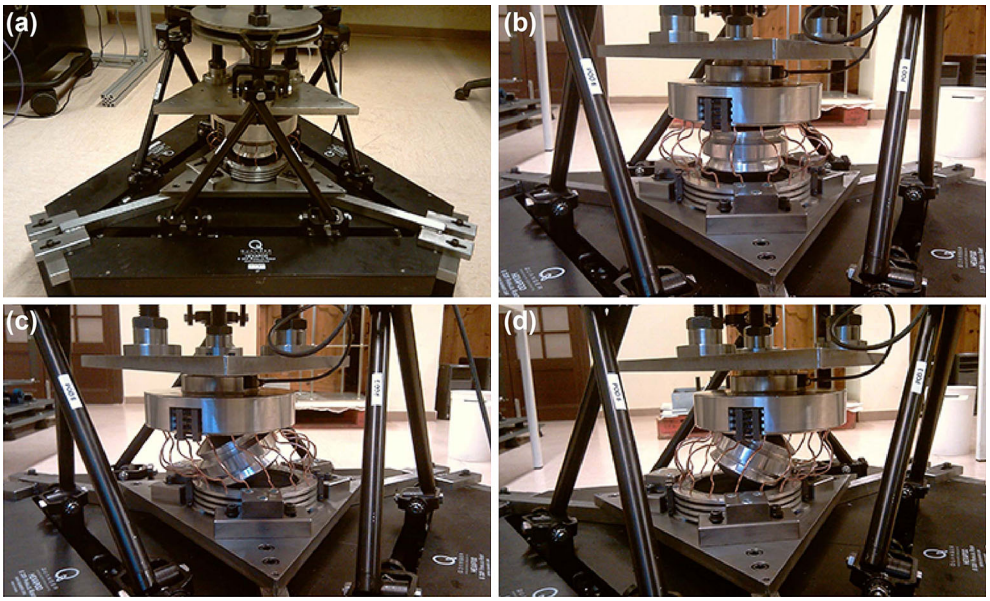

Fig. 7 **a** Mechanical extension incorporated to Hexapod; **b** neutral position; **c** to-the-left deformed position; **d** to-the-right deformed position

– Workspace (rotations about x, y and z): 36.18°, 36.18° and 50.19°;
– Maximum force (x, y and z): 1156.89, 1335.86 and 3797.62 N;
– Maximum torque (Roll, Pitch and Yaw): 548.14, 632.94 and 500.95 Nm;

An extensive series of numerical simulation tests were carried out in [15] to identify the mechanical characteristics of the RNC isolator using real-scale and small-scale prototypes numerically. These tests have been followed by thorough experimental verification using several sets of the 1/10 small-scale prototypes only of the RNC isolator having different configurations, characteristics and materials in [16]. Two samples of the used experimental prototypes are shown in Fig. 1d–e; one is made of stiff-aluminum (with a design compressive capacity of 5 kN) as shown in Fig. 1d, and the other one is made of Delrin (with a design compressive capacity of 3 kN) as show in Fig. 1e.

The lower plate of an RNC isolator prototype is tightly attached to the lower fixed base of the developed testing platform, while the upper plate of the prototype is fastened to the upper moving base of the developed testing platform, see Figs. 6 and 7. Synthetic sinusoidal and reduced-amplitude real seismic input shear displacements are applied individually (i.e., one excitation type per a laboratory experiment) to the upper moving base to generate a relative shear motion within the RNC isolator prototypes (between its top moving part and the lower fixed one). The experimental prototype responds to such relative shear displacement through rolling of the inner core and extension of the metallic yield dampers, arranged around the rolling core, as demonstrated by Fig. 7c, d. The input displacement is measured by a laser sensor to confirm that there are no losses, while the output shear force is measured by a precise force/moment sensor, which is located as shown in Fig. 6c. Two amplitudes of a chosen input shear displacement are applied to avoid activation (unscaled) and activating (scaled) the inherent buffer mechanism of the RNC isolator. To represent the results in a real sense, the reduced-scale input–output data of the reduced-scale experimental prototypes are transformed into the real scale using dimensional analysis. Two real-scale sample input–output data are plotted in Figs. 6 and 7 using synthetic sinusoidal and real seismic ground motions, respectively, and considering scaled and unscaled amplitudes to activate and deactivate the buffer mechanism, respectively.

Figure 7 anticipates the performed laboratory tests on the RNC device prototype. The monitoring system on the Hexapod allows to collect input and output quantities as reported in the following Figs. 8 and 9. They depict, respectively, the results from the sinusoidal and seismic unidirectional tests on the physical 1/10th small-scale prototype in laboratory, which has a circular shape (see Fig. 1b) with 16 metallic bars (diameter 3 mm) uniformly distributed with angular distance of 22.5° on the circumference of a circle of 188 mm in diameter. The metallic bars and the rolling body are in mild-steel with elastic modulus of 210,000 MPa,

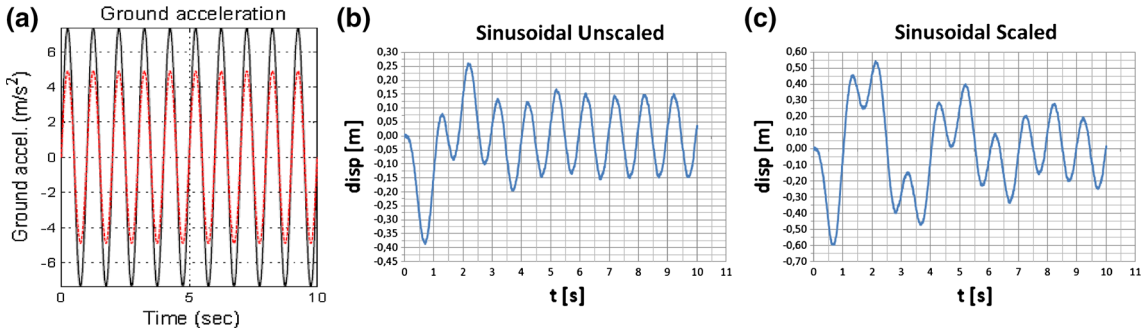

Fig. 8 Sinusoidal test. **a** Unscaled and scaled inputs. **b**, **c** Device outputs

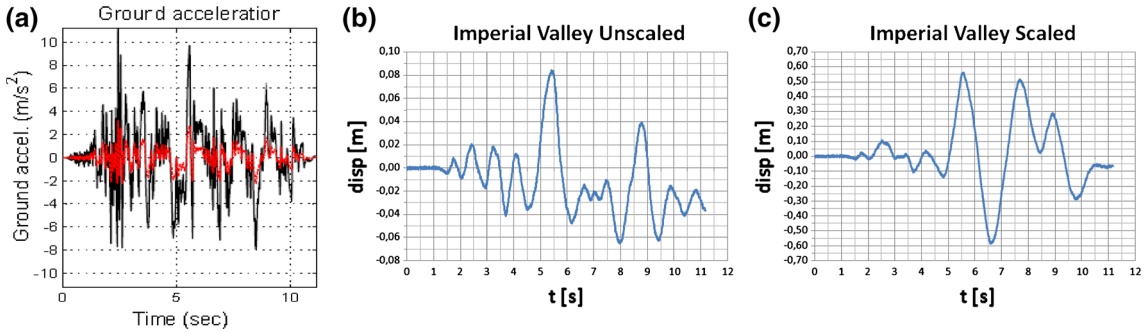

Fig. 9 Seismic test. **a** Unscaled and scaled inputs (Imperial Valley). **b**, **c** Device outputs

Poisson coefficient 0.3, yielding stress 240 MPa, post-yielding modulus 2 % of the elastic one. The geometry and the dimensions are also detailed in Fig. 2 of reference [15].

The outcomes from Figs. 8 and 9 will be useful for the modeling developments and parameters identification which will be presented in the following numerical improvements.

4 Reduced model of RNC devices

The reduced model of RNC devices introduced in this work adopts the coupled bidirectional formulation [21] initially proposed, in a different framework, by Park et al. as an expansion of the Bouc–Wen [23] monodirectional hysteretic model. The Park et al. model can be seen, as it can the Bouc–Wen one, as a black-box semi-physical model which can match an hysteretic behavior of a device by properly tuning its parameters.

In this work a modified model is used to characterize the RNC isolator device with its distinctive buffer mechanism. An independent executable program simulates the isolation devices in the structural analyses performed with the finite element commercial code ANSYS [1]. This program is to be called by the main script controlling the ANSYS analysis and is interfaced with the ANSYS database for the analysis through interface routines written in APDL (ANSYS Parametric Design Language). In particular, the process of calling the external executable from the ANSYS script is carried out using the APDL command "/SYS" [4].

4.1 Bidirectional hysteresis: basic formulations

Following the formulation in [21], the restoring force vector in a hysteretic system may be expressed as:

$$\begin{Bmatrix} q_x \\ q_y \end{Bmatrix} = \alpha[\boldsymbol{K}] \begin{Bmatrix} u_x \\ u_y \end{Bmatrix} + (1-\alpha)[\boldsymbol{K}] \begin{Bmatrix} Z_x \\ Z_y \end{Bmatrix} \tag{1}$$

in which u is the displacement vector with orthogonal components u_x and u_y, in x and y directions, respectively; q the restoring force vector with components q_x and q_y; $\boldsymbol{K}$ is the initial stiffness matrix; α is the post-yielding stiffness ratio; Z represents the hysteretic displacement vector.

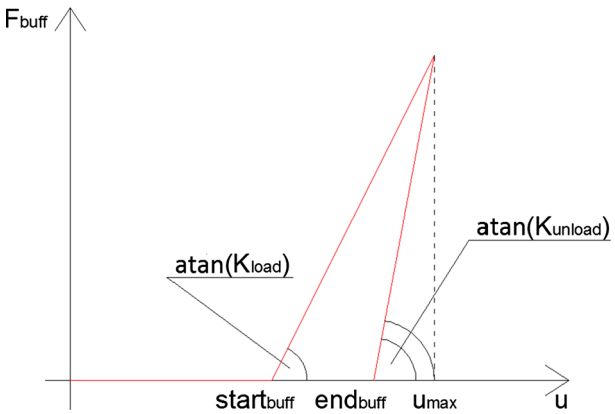

Fig. 10 Model of the buffering mechanism in the RNC device where "atan" stands for the inverse of the *tangent* trigonometric function

For isotropic hysteretic restoring forces, Z_x and Z_y satisfy the following coupled differential equations:

$$\dot{Z}_x = A\dot{u}_x - \beta|\dot{u}_x Z_x|Z_x - \gamma\dot{u}_x Z_x^2 - \beta|\dot{u}_y Z_y|Z_x - \gamma\dot{u}_y Z_x Z_y, \tag{2}$$

$$\dot{Z}_y = A\dot{u}_y - \beta|\dot{u}_y Z_y|Z_y - \gamma\dot{u}_y Z_y^2 - \beta|\dot{u}_x Z_x|Z_y - \gamma\dot{u}_x Z_y Z_x, \tag{3}$$

where A, β, γ are non-dimensional parameters that control the shape and size of the hysteresis cycle.

4.2 Mathematical modeling of the buffer mechanism

The RNC device has a peculiar built-in buffer mechanism that needs to be modeled along with its hysteretic behavior to fully characterize the isolator device.

Guided from physical experimentation of a prototype device [11], the amount of the total restoring force due to the buffer mechanism, for a monodirectional load path, may be expressed as (see Fig. 10):

$$F_{\text{buff}} = \begin{cases} 0, & u \le start\_buff \\ K_{\text{load}}(start\_buff - u) & u > start\_buff \quad \text{and} \quad \dot{u} > 0 \\ K_{\text{unload}}(end\_buff - u) & u > end\_buff \quad \text{and} \quad \dot{u} < 0 \\ 0 & u < end\_buff \quad \text{and} \quad \dot{u} < 0 \end{cases} \tag{4}$$

where F_{buff} is the buffer restoring force, K_{load} and K_{unload} are the loading and unloading stiffness, *start_buff* is the displacement (device feature) which lets the buffer mechanism start (when the rolling body and the less stiff plate are just in touch), while *end_buff* is the displacement, valued imposing the buffer force in the unloading path equal to zero, for which the buffer effect stops and the restoring force returns to be just the hysteretic one. The end buffer displacement depends not only on both stiffness and *start_buffer* displacement, but also on the maximum displacement $u_{\max}$ reached in the current loading path:

$$end\_buff = \frac{(K_{\text{unload}} u_{\max} - K_{\text{load}}\,(u_{\max} - start\_buff))}{K_{\text{unload}}}. \tag{5}$$

A new loading path is started each time u comes to be less than *start_buff*. In this case both $u_{\max}$ and *end_buff* are restored to their initial values: $u_{\max}$ = *end_buff* = *start_buff*.

This formulation has pointed out a great accordance with the results of the physical tests, as shown in the following section. When the loading path becomes bidirectional, the previous expressions can be applied with $u = \text{sqrt}(u_x^2 + u_y^2)$. In this case, the force in the radial direction due to the buffer can be easily transformed in its X and Y components.

4.3 Parameters identification

Two different identification procedures are performed in this work: one based on experimental results, coming from laboratory tests made for the very first time on a physical small-scale prototype (1/10th) of the RNC isolator (Figs. 8 and 9 in particular), and other one based on numerical simulations carried out on an FEM model of the device. A constrained nonlinear least square optimization algorithm, available in MATLAB [18], is used to obtain the model parameters in both procedures.

4.3.1 Optimization algorithm

The least square curve fitting function *lsqnonlin* is chosen from the ones available in the MATLAB Optimization toolbox. The algorithm requires the user-defined function to compute the vector-valued function:

$$f(x) = \begin{bmatrix} f_1(x) \\ f_2(x) \\ \vdots \\ f_n(x) \end{bmatrix}. \tag{6}$$

Then, in vector terms, this optimization problem can be restated as:

$$\min_x ||f(x)||_2^2 = \min_x (f_1(x)^2 + f_2(x)^2 + \cdots + f_n(x)^2). \tag{7}$$

Within this study, the function to minimize is represented by the difference between the device restoring force vector, given by the test results, q_{test}, and those of the proposed mathematical model, q_{math}, with their two in-plane components, $f_1 = (q_{\text{test},x} - q_{\text{math},x})$ and $f_2 = (q_{\text{test},y} - q_{\text{math},y})$. It can also be summarized as follows:

$$f = \begin{bmatrix} f_1 \\ f_2 \end{bmatrix} = (q_{\text{test}} - q_{\text{math}}) = \begin{bmatrix} q_{\text{test},x} - q_{\text{math},x} \\ q_{\text{test},y} - q_{\text{math},y} \end{bmatrix}. \tag{8}$$

The vectors defining the lower and upper bounds of the parameters to identify have been set taking into account what is reported in [21,23].

4.3.2 Identification from laboratory tests

The identification of the Park et al. model parameters to reproduce the RNC behavior was based on experimental results [11] coming from laboratory tests made for the very first time on a physical small-scale prototype of the RNC isolator at the Control, Dynamics and Applications Laboratory (CoDAlab), UPC, Barcelona. The tests were made, using dimensional analysis, on a small-scale (1/10th) prototype of a real-scale isolator (see Figs. 6, 7). Two different acceleration histories were given as input to the physical prototype: the sinusoidal one in Fig. 8 and the one recorded during the Imperial Valley earthquake, in Fig. 9. The inputs were afterward scaled to activate the built-in buffer mechanism of the RNC device.

The Park et al. model parameters (A, β, γ, α, K) and the buffer mechanism parameters (K_{load}, K_{unload}) identified form the experimental data with the procedure described in Sect. 4.3) are listed in Table 1, while Fig. 11 shows the match between the Park et al. model (using the parameters in Table 1) and the experimental outcome from the testing of the physical prototype in the case of activation of the buffer mechanism.

Table 1 Parameters of Park et al. model

Parameter of Park et al. model	Value
A	0.8081
K	7920.1 kN/m
α	0.0435
β	2592.1
γ	2591.1
start_buff	50 cm
K_{load}	5003.9 kN/m
K_{unload}	5215.4 kN/m

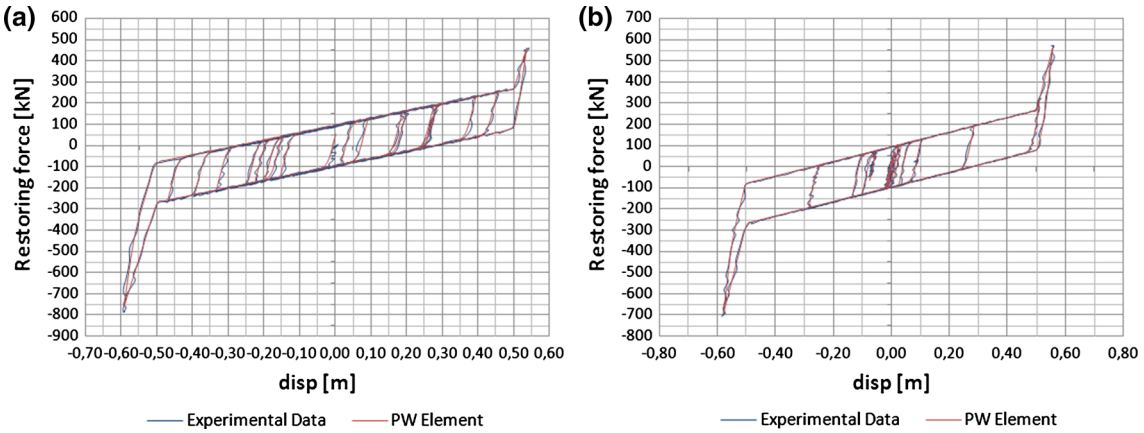

Fig. 11 Match between Park et al. model with the identified parameters in Table 1 and the experimental data from the physical test of the RNC device when buffering mechanism is activated: **a** sinusoidal input; **b** Imperial Valley input

It is worth noting that the match is satisfying for both the sinusoidal and the Imperial Valley input, even though only the sinusoidal one was used for the identification procedure, and consequently the Imperial Valley serves the purpose of a blind test.

4.3.3 Finite element reproduction of bidirectional loading paths

Testing of isolation devices is traditionally uniaxial because of the complexity of loading in two directions. However, the earthquake response of an isolated bridge deck is two-dimensional, hence bidirectional characterization of the devices is crucial in order to understand the behavior and evaluate the efficacy of the devices and of their numerical models. In light of this observations, this section is devoted to deepen this aspect for the RNC isolator device.

The only components of the RNC device which exhibit a dissipative hysteretic behavior are the metallic bars surrounding the quasi-elliptical rotating body [15]. Depending on the initial configuration (initial curvature) and the displacement histories, they can lead to a peculiar response that should be avoided at the design phase. Should this not be feasible we will in the following provide a method to include it into the Park et al. model.

To evaluate the response of the RNC to bidirectional excitations in the horizontal plane, a 3D finite element model of the dissipative bars system has been first developed in the commercially available finite element ANSYS program [1,15] by consolidated numerical procedures such as an isotropic elastic-plastic material and kinematic bidirectional hardening for the mild-steel (elastic modulus 210,000 MPa, Poisson coefficient 0.3, yielding strength 240 MPa, post-yielding modulus 2 %), isoparametric eight-nodes brick elements, geometric nonlinearities.

To assess the effects (if any) of mesh dependency, different finite element sizes and element types have been used. The presence of the rolling body, and the related contact problems between surfaces, has been disregarded. Rotations of the top surface can be neglected and the distance between the top and bottom surface of the system is constant. The degrees of freedom for the nodes of the damping bars are restrained with a body constrain to the master node, while the base of each bar has been completely restrained. The kinematic boundary conditions imply that the master node only translate in an horizontal plane.

Different finite element sizes and element types used to asses the eventual presence of mesh dependency, triggered by nonlinear behavior of materials, make reference: the first to Timoshenko beam elements (ANSYS beam188 element [1]); the others to hexahedral solid elements (ANSYS solid45 element [1]). A reasonable equivalence in the results has been reached, and the model depicted in Fig. 12a has been considered the reference one. Figure 12b depicts the detail of the slave nodes at the top of a metallic bar.

The finite element model has been subjected to several kinematic histories to obtain displacements–forces curves. In turn, these curves have been assumed as the target behaviors to be reproduced through the Park et al. law for further implementation on the bridge structural system [15]. First, the bidirectional displacement path shown in Fig. 12c was applied to the finite element model, and the displacements' history is assigned to the master node positioned in the center of the bars system. The first branches of the displacement paths are unidirectional to allow for calibrating the parameters of a Bouc–Wen model to be used for uniaxial hysteretic

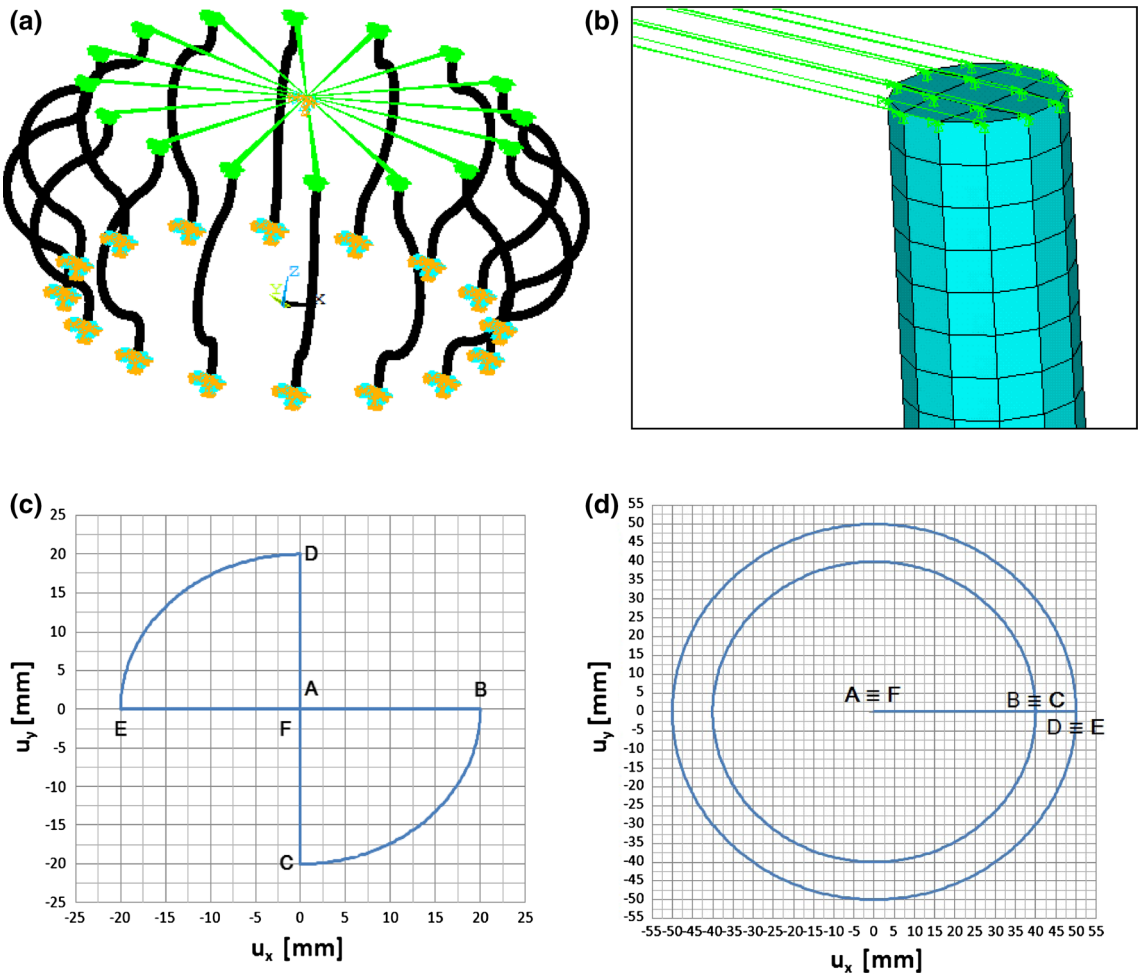

Fig. 12 Consolidated FE model (**a**), slave nodes at the top of a metallic bar (**b**), anti-symmetric (**c**) and circular displacement paths

cycles and in a simplified solution prior adopted. In that, two Bouc–Wen unidirectional models are employed together in an orthogonal uncoupled scheme, as in [15]. The results from the bidirectional analysis coming from the finite element ANSYS program are compared to the outcomes from the bidirectional model developed from the Park et al. model, and to those from the simplified solution based on two Bouc–Wen unidirectional models, in Fig. 13. This figure reports the comparison at a selected low level of displacements. Similar outcomes can been observed from both solutions with respect to the target, represented by the finite element model output.

Figure 14 shows a similar comparison, but for larger imposed displacements obtained from having scaled the displacement path in input. From this picture, one senses that a Park et al. model, set-up with constant parameters, is not able to match some peculiar features of the device behavior related to the buckling of the metallic dampers. Buckling that occurs in the unloading branch, after having reached the tensile plastic range during the loading branch (see the limit conditions in Fig. 7c, d). To overcome this deficiency, in the following, a modification of the Park et. al. model is presented based on taking into account the separate variation of the parameter α in the equations of the system (1). Therefore, this variation is expressed in both x-direction and y-direction (with $i = x, y$ and $j = y, x$), during the loading steps for the generic time instant t_k, as follows:

$$\alpha_i(t_k) = \begin{cases} \alpha, & u_i(t_k) < u_\mathrm{h} \\ \alpha + C(u_i(t_k) - u_\mathrm{h}), & u_i(t_k) \geq u_\mathrm{h} \text{ and } u_i(t_{k-1}) \leq u_\mathrm{h} \text{ and } u_j(t_k) = 0 \\ \alpha_i\,(t_{k-1}) + C\,(u_i\,(t_k) - u_i\,(t_{k-1}))\,, & u_i\,(t_k) \geq u_\mathrm{h} \text{ and } u_i\,(t_{k-1}) > u_\mathrm{h} \text{ and } u_j\,(t_k) = 0 \\ \alpha + C\,(u_i\,(t_k) - u_\mathrm{h})\,/2, & u_i\,(t_k) \geq u_\mathrm{h} \text{ and } u_i\,(t_{k-1}) \leq u_\mathrm{h} \text{ and } u_j\,(t_k) \neq 0 \\ \alpha_i\,(t_{k-1}) + C\,(u_i\,(t_k) - u_i\,(t_{k-1}))\,/2, & u_i\,(t_k) \geq u_\mathrm{h} \text{ and } u_i\,(t_{k-1}) > u_\mathrm{h} \text{ and } u_j\,(t_k) \neq 0 \end{cases} \quad (9)$$

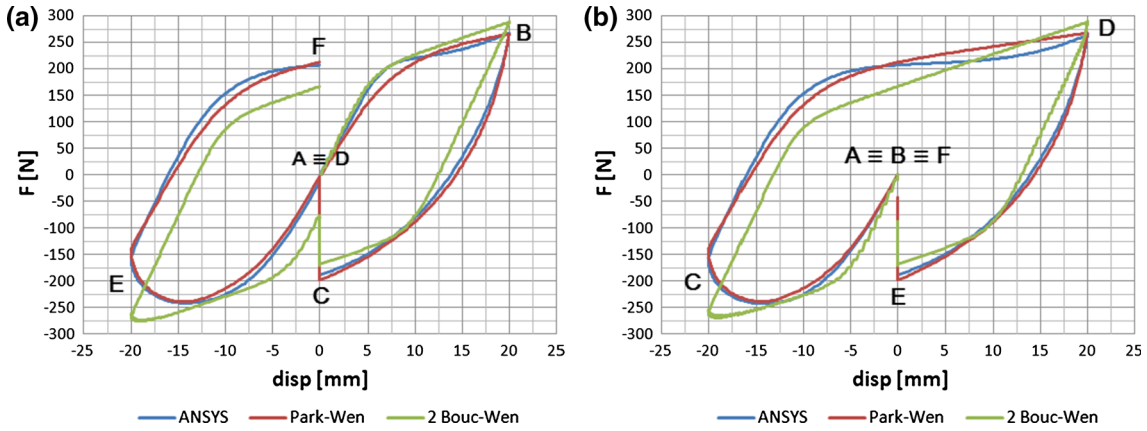

Fig. 13 Match between Park et al. model, ANSYS results and the device characterization previously adopted by the research group based on two independent Bouc–Wen models: **a** x-direction; **b** y-direction (loading path in Fig. 12c)

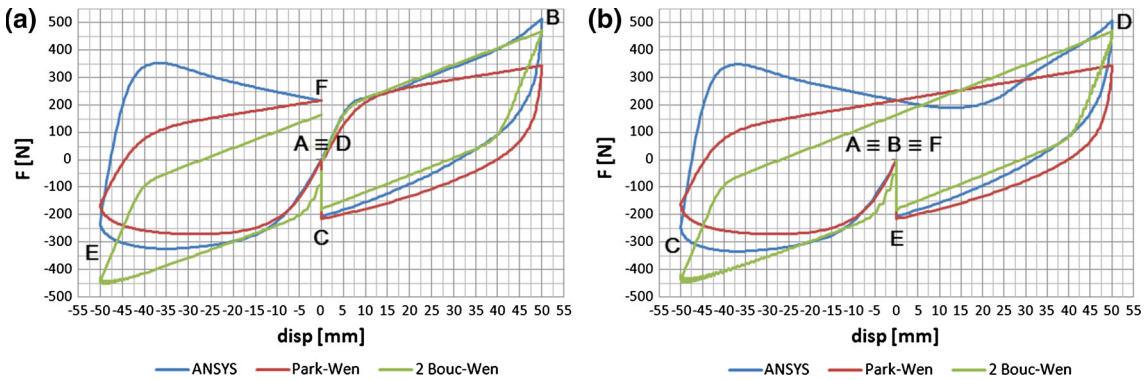

Fig. 14 Match for the scaled load path between Park et al. model, ANSYS results and the device characterization based on two independent Bouc–Wen models: **a** x-direction; **b** y-direction (loading path in Fig. 12c)

while for the unloading steps it becomes:

$$\alpha_i\,(t_k) = \begin{cases} \alpha, & u_i\,(t_k) < u_{\mathrm{h}} \text{ and } (u_j\,(t_k) \neq 0 \text{ or } u_{\max,i} < u_{\mathrm{b}}) \\ \bar{\alpha}_i - (\bar{\alpha}_i - \alpha)\,\frac{(u_i(t_k) - u_{\max,i})}{(u_{\mathrm{h}} - u_{\max,i})}, & u_i\,(t_k) \geq u_{\mathrm{h}} \text{ and } (u_j\,(t_k) \neq 0 \text{ or } u_{\max,i} < u_{\mathrm{b}}) \\ -\alpha, & u_i\,(t_k) < u_{\mathrm{b}} \text{ and } (u_j\,(t_k) = 0 \text{ and } u_{\max,i} > u_{\mathrm{b}}) \\ \bar{\alpha}_i - (\bar{\alpha}_i + \alpha)\,\frac{(u_{\max,i} - u_i(t_k))}{(u_{\max,i} - u_{\mathrm{b}})}, & u_i\,(t_k) \geq u_{\mathrm{b}} \text{ and } (u_j\,(t_k) = 0 \text{ and } u_{\max,i} > u_{\mathrm{b}}) \end{cases} \tag{10}$$

In Eqs. (9) and (10), u_{h} is the displacement at which the hardening behavior commences due to a more straight configuration of the metallic dampers, u_{b} is the displacement which takes into account the above-mentioned buckling effects, C is a constant that regulates the linear variation of α while $\bar{\alpha}_i$ is the maximum value of α reached during the loading path.

It can be noted that the occurring hardening is approximated linearly with a slope equal to C: it is also diversified in a simple way for monodirectional hardening (lines 2 and 3 of Eq. (9)) and bidirectional hardening (lines 4 and 5 of Eq. (9)).

In the unloading path, the parameter α, after having reached its peak value , would go back to its original value (line 2 of Eq. (10)), unless buckling of the bars, noticed only in the monodirectional unloading, occurs: in this case the parameter would drop to a negative value $(-\alpha)$ with a linear trend, controlled by the displacement u_{b} (line 4 of Eq. (10)).

Figure 15a, b depicts the results obtained with this model refinement that allows to correctly match the device response also at larger displacements limit.

The three further parameters introduced in this formulation (u_{h}, C, u_{b}) have been identified with the *lsqnonlin* algorithm, following the same procedure described previously in this section. The identified values are: $u_{\mathrm{h}} = 19.41$ mm, $C = 0.00002609$, $u_{\mathrm{b}} = 43.04$ mm.

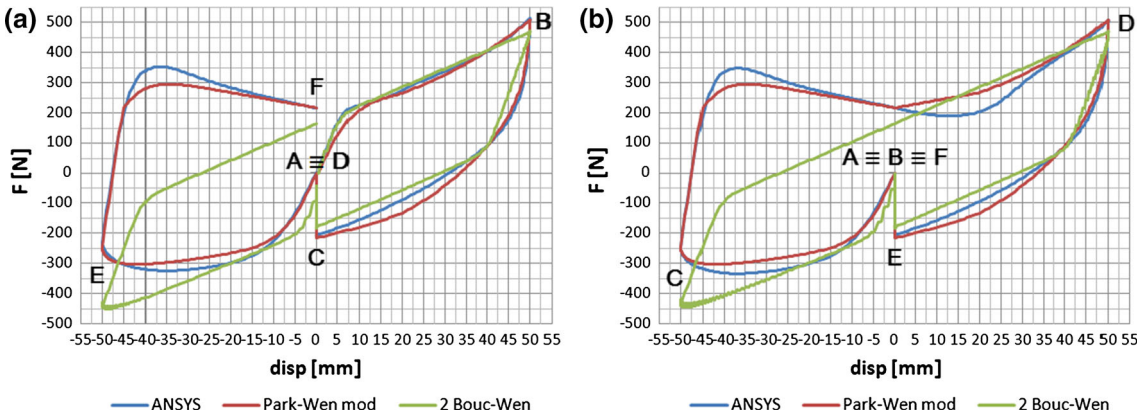

Fig. 15 Match for the scaled load path between the modified Park et al. model, ANSYS results and the device characterization based on two independent Bouc–Wen models: **a** x-direction; **b** y-direction (loading path in Fig. 12c)

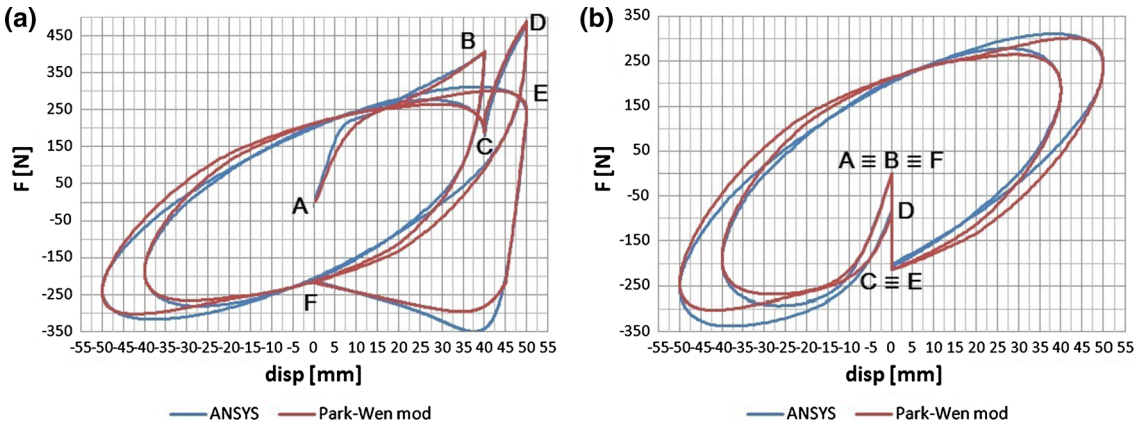

Fig. 16 Comparison between the modified Park et al. model and the ANSYS FE model results for the loading path of Fig. 12d: **a** x-direction; **b** y-direction

The relevance of the modified Park et al. model, herein proposed, has also been assessed with reference to another significant bidirectional loading path pattern, widely used in literature, shown in Fig. 12d. The model response is presented in Fig. 16 which highlights how, also for this case, the model's refinement is able to properly reproduce the device response predicted from the FE model at larger displacements values.

5 Updated bridge benchmark model and seismic action

The bridge under study is a 1206-m-long, fan-type cable-stayed bridge (Fig. 17), which crosses the Mississippi River near Cape Girardeau (USA), connecting Illinois and Missouri. The main span length is 350.6 m. The deck is of mixed construction concrete-steel and is stiffened by longitudinal steel girders.

One hundred and twenty-eight stays of high-strength, low-relaxation, steel, arranged in a fan-type configuration, support the deck. The smallest cable ha a cross-sectional area of 28.5 cm^2, while the largest one has cross-sectional area of 76.3 cm^2. The cable-stayed spans are supported by two towers, while twelve additional piers support the Illinois approach spans. Each tower has a solid section below the cap beam, and a hollow section in the upper portion. For a more detailed description of the structure, as well as of its members, the reader is referred to [2].

This bridge was the subject of a well-known benchmark on bridge control [2]. The model of the cable-stayed bridge adopted is set-up [5,6,15,18] in the ANSYS finite element framework enhancing the original benchmark model moving from a single rod-type representation for each cable to a description with six rope elements per cable. This is to improve the modeling of the stays-deck coupled response. Furthermore, the nonlinear response of the structure is also accounted for by evaluating the dynamic equilibrium of the structure

Fig. 17 The Bill Emerson Memorial Bridge (Framerotblues 2007; with permission)

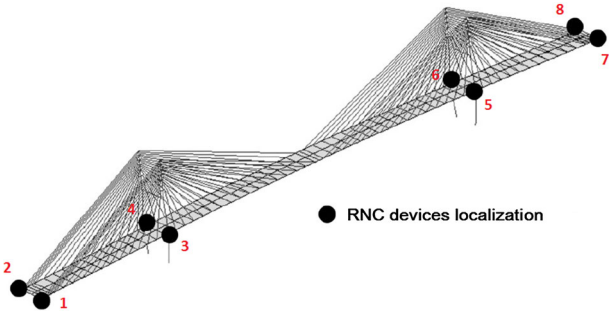

Fig. 18 The Bill Emerson Memorial Bridge FEM model. The *black dots mark* the positions where RNC devices were added to the numerical model

in the deformed configuration at any instant of the simulations. Additionally, the numerical model [8,15] comprises soil–structure interaction (in the vertical, transversal and longitudinal direction) through the use of impedance functions, lumped masses, springs and dampers at bents and piers.

The resulting finite element mesh in ANSYS comprises (Fig. 18) linear beam elements for towers and the deck frame, linear shells elements for the concrete deck slab, tension only elements for the stay cables, totaling about 2600 nodes and 2800 elements. The materials are characterized as linear elastic. High performance concrete is adopted for the piers ($E = 50 \times 106\,\text{kN/m}^2$); high-strength, low-relaxation steel for the stay cables ($E = 210 \times 106\,\text{kN/m}^2$). The mixed structure of the deck (steel frame with concrete slab) is modeled by concrete shell elements connected to steel beams. The two materials retain the specified characteristics. A structural damping appropriate to this type of bridges (equal to 3 % of the critical one) is assigned to the bridge model as a Rayleigh-type damping computed between the first (0.28 s) and the sixth (0.64 s) modes.

Soil–structure interaction is included in the bridge model. The ground motion is applied to the structure in the form of free-field ground displacements and velocities. These have been obtained from synthetic generated acceleration time-histories, considering the spatial variability of the seismic ground motion. The acceleration time-histories are obtained by the procedure presented in [19,20], which relies on the spectral representation method by Shinozuka [22]. At the structure–soil contact points the auto-spectrum of the generated accelerations satisfy the well-known Kanai–Tajimi power spectral density (PSD) as modified by Clough and Penzien [3], while the cross-spectra between the motions at different stations are derived from the coherency function proposed by Luco and Wong [17]. In the case at hand, a velocity of the shear waves $v_s = 3000$ m/s and an incoherency factor $\alpha = 0.2$ were adopted. Distinctively, the parameters of the Clough and Penzien PSD are chosen in order to minimize the difference between the value of the median response pseudo-acceleration spectrum with that prescribed by Eurocode 8 (EC8) [9]. Figure 19a, b depicts the average, over ten realizations, pseudo-acceleration spectra with those imposed by EC8 for the horizontal and vertical component, respectively. The spectra are normalized to get a peak ground acceleration of 1 m/s^2.

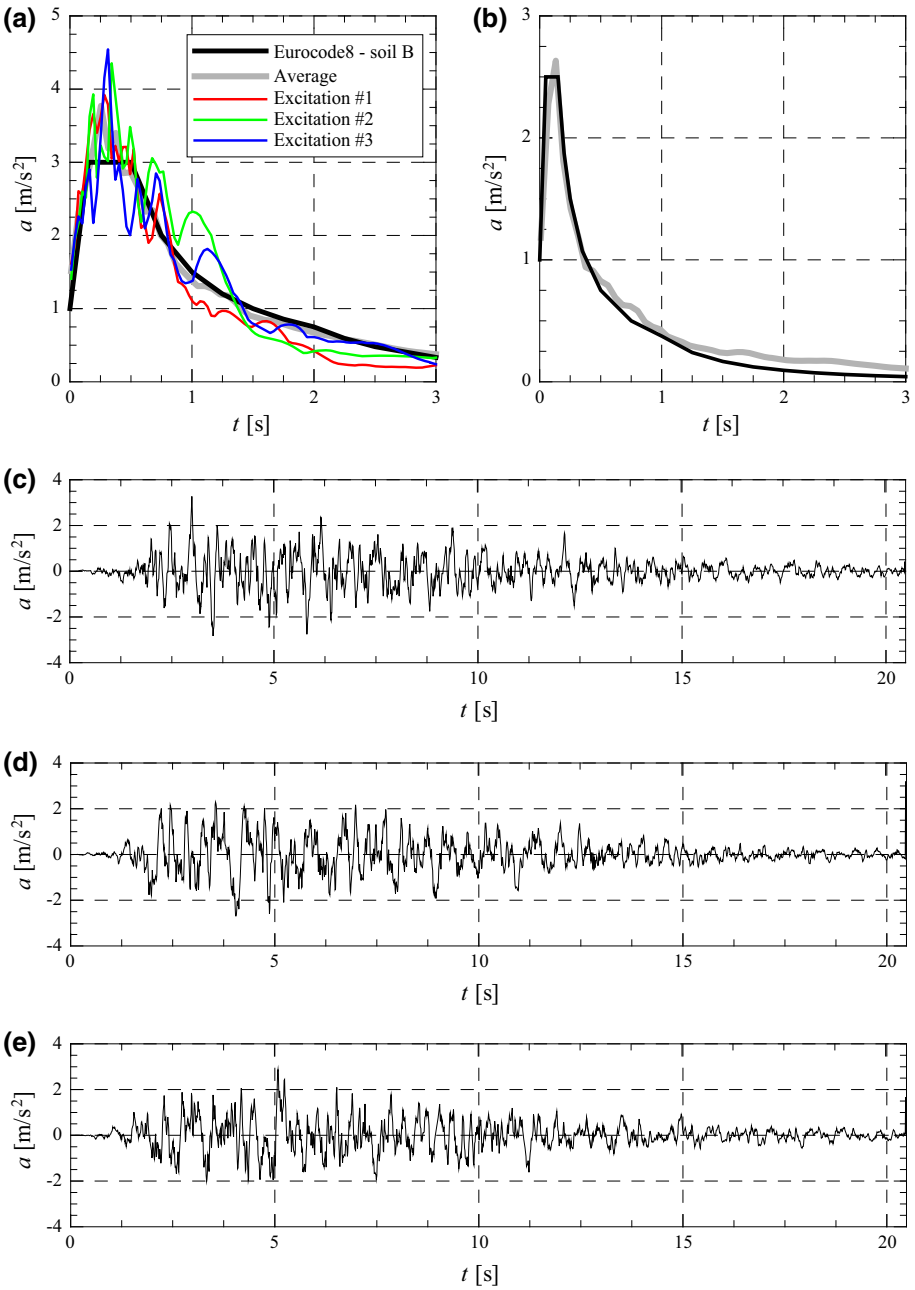

Fig. 19 Average pseudo-acceleration spectra computed from ten realizations of the ground motion for: **a** horizontal component of ground acceleration, **b** vertical component. Longitudinal acceleration at left bent for: **c** Excitation #1, **d** Excitation #2, **e** Excitation #3

6 Seismic performance of RNC on the bridge structure

Eight RNC devices are introduced in the bridge model, symmetrically with respect to the longitudinal axis, between deck and bents, and deck and piers at the locations highlighted by a black dot in Fig. 18. The isolators correspond to the full-scale RNC device tested, since, referring to previous works [15], the parameters for this device are included in the optimal range of protection for the analyzed structure. The parameters for the reduced model are those in Sect. 3.

The technique summarized in the previous section for generating the horizontal and vertical component of ground motion has been used to generate ten different excitations compatible with the horizontal response

Table 2 Criteria for assessing the performance of the isolation system

Criterion	Response parameter
H1	Maximum tower base bending moment about the longitudinal direction
H2	Maximum tower base torque
H3	Maximum tower base bending moment about the transversal direction
H4	Maximum tower base shear in longitudinal direction
H5	Maximum tower base shear in transversal direction
H6	Maximum mid-deck displacement in longitudinal direction
H7	Maximum mid-deck displacement in transversal direction
H8	Maximum longitudinal mid-deck acceleration
H9	Maximum transversal mid-deck acceleration

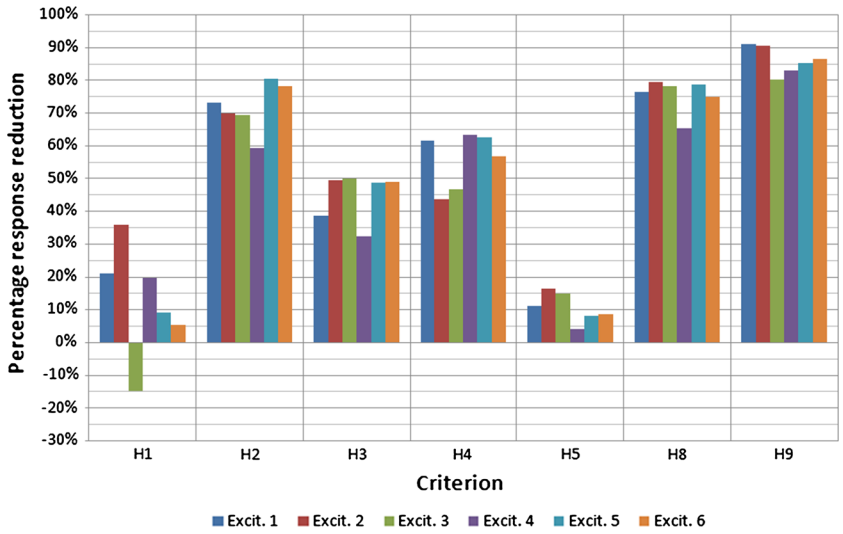

Fig. 20 Percentage reductions for some of the assumed performance criteria in Table 2 computed on the controlled and uncontrolled bridge configurations

spectrum and 10 with the vertical response spectrum specified by EC8 for soil-type "B". Each time-history can be seen as a statistically independent realization of a stochastic process described by an appropriately modified Clough and Penzien [3] PSD to become spectrum-compatible. As such, two different realizations belong to a population that has the EC8 prescribed spectra as the average, and they are completely uncorrelated and only share the time envelope function used to make them non-stationary in time (a sample is shown if Fig. 19c, d). The average acceleration response spectra, normalized at a PGA of 1 m/s^2, for the time-histories representing the horizontal ground motion and the vertical ground motions are depicted in Fig. 19a, b, respectively. In Fig. 19a, the response spectra for the horizontal accelerations at the left bent in Excitations #1–#3 are shown as well. Figure 19c, d depicts the longitudinal, with respect to the bridge, acceleration at the left bent for the same excitations.

Six analyses were carried out in the time domain (Excitation #1–#6), each one obtained by pairing two different seismic inputs in the horizontal direction and one in the vertical direction obtained as briefly described in the previous section. Comparisons between the two different bridge configurations (controlled and uncontrolled) will be shown in the following, in terms of average percentage reductions for the criteria listed in Table 2.

Figures 20 and 21 summarize the outcomes of the numerical analyses on the bridge numerical model protected with RNC devices. The histograms in these figures represent the percentage reductions, with respect to the uncontrolled bridge configuration, for the assumed performance criteria. Figure 20 shows the results for evaluation criteria related to internal forces, while Fig. 21 shows those related to displacements. The two sets have been kept separated to improve readability since have a vastly different range of values. Positive values mean an actual reduction in the response for the controlled configuration, negative values an increase.

Internal forces at the tower base (H1–H5) are generally reduced even if some differences arise. In the longitudinal direction, the control system results more effective, showing up to 60 % of reduction in the

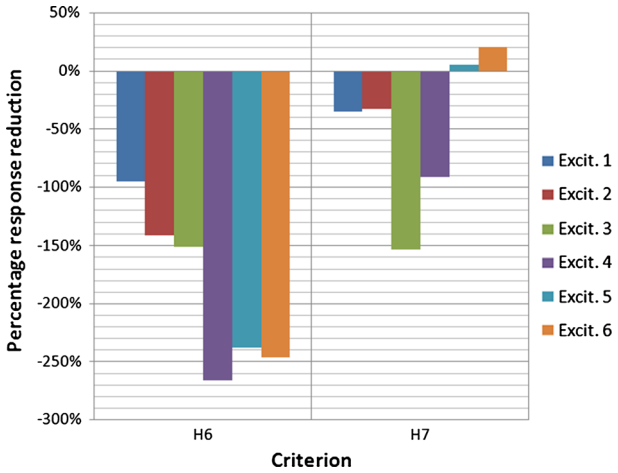

Fig. 21 Percentage reductions for some of the assumed performance criteria in Table 2 computed on the controlled and uncontrolled bridge configurations

Table 3 Comparison with and without buffer mechanism, input #6

Criterion	Relative difference (%)
H1	0.02
H2	4.99
H3	0.05
H4	0.00
H5	−0.06
H6	−6.00
H7	0.00
H8	3.89
H9	−1.34

controlled system with respect to the uncontrolled configuration of the bridge. Accelerations at the mid-span of the deck are also essentially reduced by the control system which operates releasing the relative motion between the bridge deck and the supports (H8, H9).

The improved performance of the bridge arrangement in terms of internal actions is reached at the cost of increments in the relative displacements (H6, H7). In light of this consideration, it is also worth noting that the reduction in internal forces in the longitudinal direction (e.g., H3, H4), with respect to the transversal direction (e.g., H1, H5), is mirrored by the displacements increments, with higher values in longitudinal direction (H6) with respect to the transversal one (H7).

Even if the buffer bidirectional formulation has to be confirmed by further physical tests, the monodirectional results and the consistent approach, with respect to the Park et al. model, justifies its use on the bridge model. Therefore, for Excitation #6, Table 3 reports a coherent (same structural conditions) comparison in terms of relative difference for the criteria in Table 2 when the buffer mechanism in the RNC devices is excluded or included in the model. A small reduction in the longitudinal displacements (criterion H6) is reached when displacements are limited by the buffer mechanism of the RNC devices, with respect to the condition without buffer mechanism. This result is achieved at the cost of a small increment of the longitudinal acceleration of the deck (criterion H8). The remaining criteria do not show sensible variations.

Finally, aiming at a comparison with a previous study [15] on the bridge where the RNC devices were simulated by two orthogonal–unidirectional–uncoupled Bouc–Wen models, a comparison has been performed with the bridge model in [15] equipped with RNC devices simulated by the bidirectional model with buffer herein formulated. Table 4 lists, for seismic input #4 and #5, the relative difference for the criteria listed in Table 2 coming from the two modeling approaches. It is worth underlining that the input #4 is characterized by a strong bidirectional signature, much larger than for input #5. Indeed, from Fig. 22 which shows X and Y displacements for input #4 and #5, it can be noted how the first one has roughly the same displacements values in directions X and Y, while the second has a maximum displacement in direction X (the main direction of ground motion) about tree times that in direction Y.

Table 4 Comparison between monodirectional and bidirectional formulation for the RNC device in the bridge model

Criterion	Input #**4** Relative difference (%)	Input #**5** Relative difference (%)
H1	19.70	−0.53
H2	−54.92	−12.85
H3	−8.65	−1.82
H4	−33.61	−0.45
H5	−5.19	0.26
H6	−33.80	−25.24
H7	−105.92	−24.95
H8	21.47	−10.66
H9	−310.00	−7.71

Values are computed as -((Hi_{BW} − Hi_{PW})/Hi_{PW}), with i the criterion, BW the value from the monodirectional formulation, PW the value from the bidirectional formulation

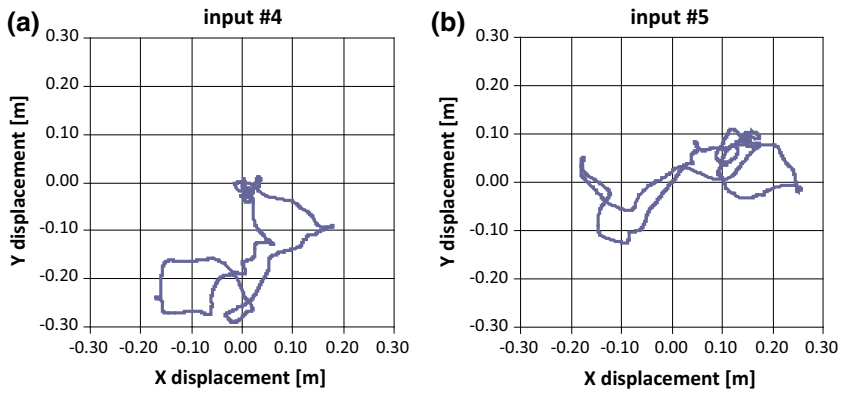

Fig. 22 X and Y displacement time-histories for input #4 (**a**) and for input #5 (**b**)

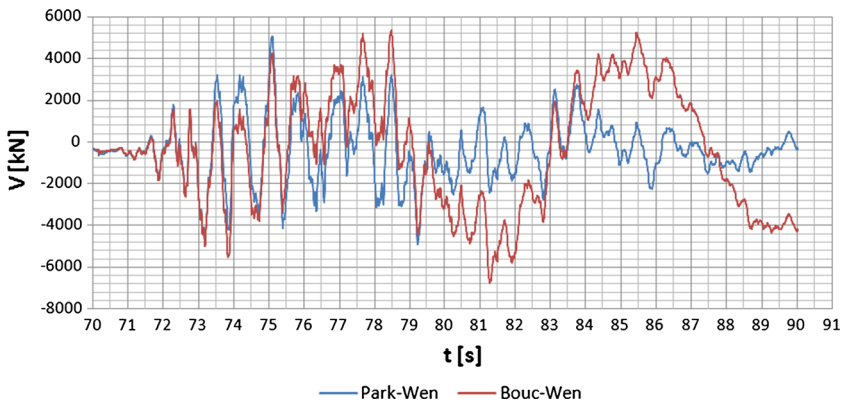

Fig. 23 Base shear in longitudinal direction at one of the towers' bases, for Excitation #4

One can observe from the values in Table 4 that a monodirectional modeling can not precisely follow the actual behavior of the isolator when this is affected by a non-negligible interaction in the two orthogonal direction. To further highlight the differences between the two approaches in time domain, Fig. 23 shows, for Excitation #4, the time-history of the base shear in longitudinal (with respect to the deck development) direction at the base of the tower closer to the Illinois side. On the contrary, when the bidirectional effects are less important (input #5), both approaches perform similarly.

7 Conclusions

The laboratory tests and the analyses performed as part of this work offer an insight into the development of an innovative isolation device. The physical model of the RNC device successfully tested using a Hexapod-based laboratory facility in unidirectional orthogonal loading paths, confirmed the specific characteristics of the dampers, as were identified by previous design studies. The laboratory tests allowed to confirm the preliminary design studies and to validate a new bidirectional model able to precisely follow the actual behavior of the isolator.

The laboratory tests and analyses performed lead to the following specific conclusions:

- The modified Park et al. model with optimal tuning of the parameters was proved able to match satisfactorily the physical behavior of the RNC. The same phenomenological model confirms to be effective also in reproducing the bidirectional response of the 3D finite element model of the dampers, including buckling of the same. This outcome will be very useful in planning and conducting further experiments on the physical model of the RNC isolator when bidirectional loading paths will be fully employed on the Hexapod facility.
- The RNCs devices, numerically simulated in the bridge analyses, were able to perform an effective reduction in the seismic effects both in terms of internal actions and accelerations. However, in agreement with the seismic isolation theory, this implied an increase in the displacements for the structure.
- The effect of the buffer mechanism on the bridge model slightly limits the peak displacements, at cost of a small increment of the deck accelerations. Internal forces did not show remarkable variations.
- A coupled bidirectional model (as the modified Park et al. one) is fundamental to precisely reproduce the actual behavior of the isolators when the deck motion is affected by a non-negligible interaction in the two (longitudinal–transversal) directions. Some performance criteria can vary by as much as 300 % as a consequence.

The refined version of the ASCE bridge benchmark model confirms the positive contribution of the new dissipative isolation devices in the mitigation of the seismic effects in terms of internal actions and displacements of the structural components, as already emerged from previous studies carried out with a simpler model of the RNC device. Furthermore, the specific outcomes of the buffer mechanisms and the benefits coming from a full bidirectional formulation of the damper model have been assessed.

References

1. ANSYS. Academic release 12 user manual, ANSYS, Canonsburg, Pennsylvania (2011)
2. Caicedo, J.M., Dyke, S.J., Moon, S.J., Bergman, L.A., Turan, G., Hague, S.: Phase II benchmark control problem for seismic response of cable-stayed bridges. Journal of Structural Control **10**(3–4), 137–168 (2003)
3. Clough, R.W., Penzien, J.: Dynamics of structures. McGraw-Hill, New York, NY (1975)
4. De Mari, G.: Controllo strutturale di ponti strallati mediante sistema RNC - Formulazione bidimensionale del sistema di controllo (in Italian). MSc Thesis A.Y. 2013-2014; Politecnico di Milano, Milan I (2014)
5. Domaneschi, M., Martinelli, L., Shi, C.: Aeolic and Seismic Structural Vibrations Mitigation on Long-Span Cable-Supported Bridges. Advanced Materials Research **690**(693), 1168–1171 (2013). doi:10.4028/www.scientific.net/AMR.690-693.1168
6. Domaneschi, M., Martinelli, L.: Performance Comparison of Passive Control Schemes for the Numerically Improved ASCE Cable-Stayed Bridge Model. Earthquakes and Structures; 3(2):181–201. ISSN: 2092-7614 (Print), ISSN: 2092-7622 (Online) (2012)
7. Domaneschi, M., Martinelli, L.: Extending the Benchmark Cable-Stayed Bridge for Transverse Response under Seismic Loading. Journal of Bridge Engineering ASCE 2014; 19(3). doi:10.1061/(ASCE)BE.1943-5592.0000532
8. Domaneschi, M., Limongelli, M.P., Martinelli, L.: Vibration Based Damage Localization Using MEMS on a Suspension Bridge Model. Smart Structures and Systems **12**(6), 679–694 (2013)
9. Eurocode 8 EN 1998–1. Design of structures for earthquake resistance 2005. Part 1: General rules, seismic actions and rules for buildings
10. Ismail, M., Rodellar, J., Ikhouane, F.: Method for the seismic isolation of a supported object. Patents No. WO2010000897A1, ES20080002043, P200802043, Spanish Office of Patents and Marks (2008)
11. Ismail, M., Rodellar, J.: Experimental mechanical characterization of a rolling-based seismic isolation system. In: Proc. 6WCSCM, Sixth World Conference on Structural Control and Monitoring, Barcelona, Spain (2014)
12. Ismail, M., Casas, J.R., Rodellar, J.: Near-fault isolation of cable-stayed bridges using RNC isolator. Engineering Structures **56**, 327–342 (2013)
13. Ismail, M., Rodellar, J.: A mechanical extension for Stewart platform (Hexapod). Patent No. P201331348, Spanish Office of Patents and Marks (2013)
14. Ismail, M.: An innovative isolation device for aseismic design. PhD thesis 2009; Doctoral program: Earthquake Engineering and Structural Dynamics, Technical University of Catalonia, Barcelona, Spain. (http://www.tdx.cat/handle/10803/6265), accessed 10th May 2014 20:08

15. Ismail, M., Rodellar, J., Carusone, G., Domaneschi, M., Martinelli, L.: Characterization, modeling and assessment of roll-n-cage isolator using the cable stayed bridge benchmark. Acta Mechanica **224**(3), 525–547 (2013)
16. Ismail, M., Rodellar, J.: Experimental mechanical characterization of a rolling-based seismic isolation system. In: Proc. 6WCSCM, Sixth World Conference on Structural Control and Monitoring; Barcelona, Spain (2014)
17. Luco, J.E., Wong, H.L.: Response of a rigid foundation to a spatially random ground motion. Earthq Eng Struct Dyn **14**, 891–908 (1986)
18. MATLAB. Release R2013a user manual, MATLAB, Natick, Massachusetts (2013)
19. Martinelli, L., Barbella, G., Feriani, A.: Modeling of Qiandao Lake submerged floating tunnel subject to multi-support seismic input. Procedia Engineering **4**, 311–318 (2010)
20. Martinelli, L., Barbella, G., Feriani, A.: A numerical procedure for simulating the multi-support seismic response of submerged floating tunnels anchored by cables. Eng Struct **33**, 2850–2860 (2011)
21. Park, Y.J., Wen, Y.K., Ang, K.S.: Random vibration of hysteretic systems underbi-directional ground motions. Earthquake Engineering and Structural Dynamics **14**, 543–557 (1986)
22. Shinozuka, M.: Monte Carlo solution of structural dynamics. Comput Struct **2**(5-6), 855–874 (1972)
23. Wen, Y.: Method for random vibration of hysteretic systems. Journal of the Engineering Mechanics Division ASCE **102**(2), 249–263 (1976)